ELSEVIER

Analysis of tongue and groove joints for thick laminates ☆

Karel Matouš, George J. Dvorak*

Department of Mechanical, Aerospace, and Nuclear Engineering, Centre for Composite Materials and Structures, Rensselaer Polytechnic Institute, 5003 Jonsson Engineering Center, 110 8th Street, Troy, NY 12180-3590, USA

Abstract

A finite element evaluation of local stresses in the adhesive and adherends is presented for a tongue-and-groove joint of a homogenized thick composite laminate to steel plate. The quasi-isotropic laminate is made of glass fabric/vinyl ester plies. Most results are obtained for elastic response of the Dexter-Hysol 9338 adhesive that was used in recent experiments (Compos Sci Technol 61 (2001) 1123–1142). A nonlinearly viscoelastic adhesive is also considered, with illustrative properties taken from experiments on the FM-73 system. Both in-plane force resultants and out-of-plane moments are included in the applied loads. Scaling of the elastic results with regard to plate thickness shows that for given levels of overall stresses applied to the adherend plates, the stresses supported by the adhesive do not depend on plate thickness. Adhesive stress relaxation is shown to be relatively small, and occurring in a short time period.
© 2004 Elsevier Ltd. All rights reserved.

Keywords: Adhesive joints

1. Introduction

Adhesive joining of thick composite laminates, often used in marine structures, presents problems not encountered in joining thin sections, where lap joint configurations of sufficient strength are widely used. Scaling of thin section joints by at least one order of magnitude presents two difficulties. One is related to the large doubler overlap length; for example, Hart-Smith [1] recommends overlap of $20h$–$30h$ for plate thicknesses $h = 0.125$–0.040 in. A more serious limitation is caused by the high in-plane force resultants transmitted by thick plates, which elevate the stress magnitudes concentrated at adhesive leading edges. At a certain load level, these stresses can exceed the relatively low out-of-plane shear strength of the laminate surface plies, or the peel and shear strengths of adhesive, and thus restrict the utility of lap joints to relatively thin sections.

The present paper extends our recent results [2,3] on analysis and design of tongue and groove (T&G) joint for joining thick quasi-isotropic laminated plates to metal or laminate adherends. As shown in Fig. 1, the bondline extends through the thickness of the plate. At a given magnitude of an applied in-plane stress, the stresses supported by the adhesive are independent of a plate thickness h. Resolved tractions acting at the bonded interface are now supported by the much higher in-plane strength of the laminate, hence the load-bearing capacity of the (T&G) joint is no longer limited by surface ply properties. Moreover, scaling of such joints to arbitrary plate thickness does not require any change in the in-plane size or geometry of the joint. As suggested by our experimental results [3], full strength of the tongue and grove joint in a glass fabric/vinyl-ester quasi-isotropic laminate is reached at overall length of $L_0 = 12$ in., hence this length is retained herein.

Unit magnitude in-plane force resultant and out-of-plane moment are both applied to the joint considered in the present study. Together with reshaping of the tongue leading edge for reduced adhesive stress concentration, this is described in Section 2. Then, Section 3 explains the finite element solution procedure used in solving specific problems. Section 4 outlines the constitutive relations of the non-linear viscoelastic adhesive, selected in evaluation of adhesive stress relaxation under sustained and variable loading. The results are presented in Section 5, and Section 6 describes the scaling of results to different plate thicknesses. Finally, conclusions are drawn in Section 7.

☆ Accepted for publication in Composites Part B: Engineering.

* Corresponding author. Tel: +1-518-276-6940; fax: +1-518-276-2623.
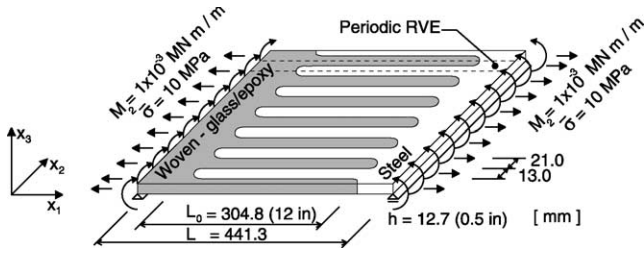 *E-mail address:* dvorak@rpi.edu (G.J. Dvorak).

Fig. 1. Geometry of steel to laminate tongue and groove (T&G) joint.

2. Problem formulation

The specific geometry and loads applied to the tongue-and-groove joint analyzed in this paper are shown in Fig. 1. The geometry is similar to that used in Ref. [3] for evaluation of the stress distribution in the representative volume element (RVE) of the joint and in the specimens used in the experimental program, but the spacing and width of the tongues have been changed. The new dimensions were evaluated in Ref. [3] (Section 4.2) as giving the highest joint efficiency (60%) for design based on maximum allowable stresses in the steel and laminate adherends. Also, both an in-plane tension stress $\bar{\sigma}_{11} = 10$ MPa and an out-of-plane bending moment $M_2 = 1 \times 10^{-3}$ MNm/m, were applied in analysis of the stresses in the adhesive and adherends, Fig. 1. The RVEs of the present joint configurations are shown in Figs. 2 and 3. The points A, B and C, D mark the semicircular endings of the grooves in the laminate and steel adherends, respectively. Since high stress concentrations would be present in an adhesive layer joining the semi-circular interface at the tip of the inserts, the leading edges of the adhesive layer were recessed into the flat part of the T&G joint, and are marked by points E and F in Figs. 2 and 3. The tapered leading edge of the steel insert in Fig. 3 was introduced for reduction of stress concentrations at the adhesive leading edge E.

Under the prescribed loads, both longitudinal edges of the RVE, labeled as Section 1-1 and Section 2-2 in Figs. 2 and 3, are planes of symmetry. As such, they are subjected to constant displacements u_2 in the direction normal to the edges. Selecting $u_2 = 0$ along Section 1-1, one can find the $u_2 = $ const. on Section 2-2 from the condition of zero transverse stress resultant on all planes $x_2 = $ const., i.e. $\int_0^L \sigma_{22} dx_1 = 0$. This integral is evaluated while the RVE is loaded by the prescribed tension stress or the bending

moment, and by at least two trial values of $u_2 = $ const. These evaluations are generally different from zero, but allow interpolations identifying the desired values of u_2 that render the integral equal to zero. Moreover, the traction components on the Section 1-1 and Section 2-2 in Figs. 2 and 3 were prescribed as $\sigma_{12} = \sigma_{23} = 0$.

Both adherends were regarded as homogenized, anisotropic elastic solids. Material properties of the adherends and adhesives prescribed in the numerical analysis were adopted, in part, from Ref. [3] and are summarized in Table 1. Response of the T&G joint was analyzed with both elastic and non-linearly viscoelastic adhesives; the latter, FM-73, was selected because its viscoelastic properties are well-known [8]. However, its performance with the present adherends was not evaluated in our experiments in Ref. [3], where the Dexter-Hysol 9339 adhesive was used.

3. Solution procedures

The representative volumes in Figs. 2 and 3 were subdivided by either three-dimensional (3D) or in-plane two-dimensional (2D) meshes. Tetrahedral 3D elements with quadratic shape functions were generated by the T3D mesh generator [5]. Over 22,200 elements were used, requiring solution to about 100,000 equations in each run. The adherend plates were subdivided by four rows of elements through the thickness of the plate in x_3 direction, and the adhesive layer was further discretized by two rows of elements in x_2 direction, with refinement at the leading edge of the bondline to capture high stress gradients.

Triangular 2D elements with linear shape functions were also generated by the T3D mesh generator [5]. Almost 15,000 elements were used, leading to over 38,000 equations. The adhesive layer was again discretized by two rows of elements, with refinement at the leading edge. In the 2D analysis, the stresses σ_{11}, σ_{22} and the in-plane shear stress σ_{12} were assumed to be linearly varying through the thickness of the adherend plates, according to Mindlin's plate theory with following kinematic assumptions,

$$u_1(x_1, x_2, x_3) = U_1(x_1, x_2) + x_3 \phi_2(x_1, x_2)$$

$$u_2(x_1, x_2, x_3) = U_2(x_1, x_2) - x_3 \phi_1(x_1, x_2)$$

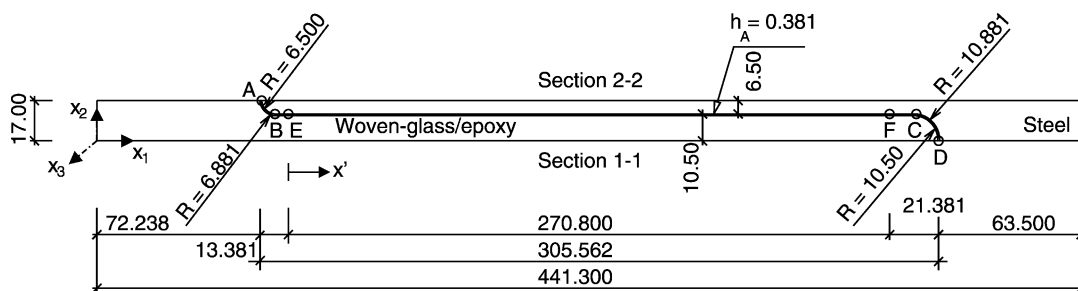$$u_3(x_1, x_2, x_3) = U_3(x_1, x_2) \tag{1}$$
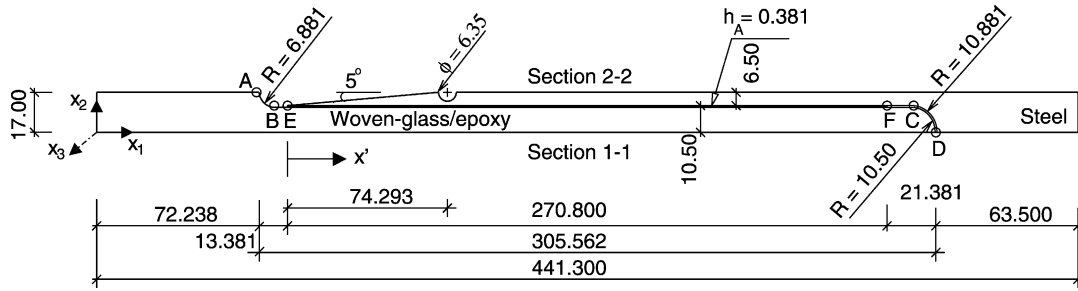

Fig. 2. Representative volume element of T&G joint.

Fig. 3. Representative volume element of T&G joint with V-notched/tapered steel insert.

where vector **U** denotes axial displacement, and the ϕ_1, ϕ_2 are rotations around the x_1, x_2 axes, respectively. The in-plane strain vector can be written in the form,

$$\boldsymbol{\varepsilon}_m = (\boldsymbol{\varepsilon}_{0m}) + x_3 \mathbf{S} \boldsymbol{\kappa}$$

$$(\boldsymbol{\varepsilon}_{0m}) = [U_{1,1}, U_{2,2}, U_{1,2} + U_{2,1}]^T$$

$$\boldsymbol{\kappa} = [\phi_{1,2}, \phi_{2,1}, \phi_{1,1} - \phi_{2,2}]^T \qquad (2)$$

where orthogonal matrix **S** is given by,

$$\mathbf{S} = \begin{bmatrix} 0 & 1 & 0 \\ -1 & 0 & 0 \\ 0 & 0 & -1 \end{bmatrix}. \qquad (3)$$

In agreement with this theory, the out-of-plane stresses σ_{23}, σ_{13} are constant through the thickness and out-of-plane strains $\boldsymbol{\varepsilon}_s = [\varepsilon_{13}, \varepsilon_{23}]^T$ are related to the displacement field by,

$$\boldsymbol{\varepsilon}_s = [U_{3,2} - \phi_1, U_{3,1} + \phi_2]^T. \qquad (4)$$

The symbols $U_{1,j}$, $\phi_{1,j}$ are used to denote partial differentiation with respect to x_j.

As expected, local stress oscillations were found at the adhesive leading edge. These were not investigated in detail; instead the adhesive layer stresses were evaluated in terms of thickness averages,

$$\sigma_{ij}^{\text{average}} = \frac{1}{h^A} \int_0^{h^A} \sigma_{ij}^{\text{element}} dx_2. \qquad (5)$$

where h^A denotes the thickness (0.381 mm) of the adhesive layer; singular stresses located in a very small volume were omitted.

It is shown below that the 2*D* analysis appears adequate for the joint problems considered herein, and offers certain advantages over its 3*D* counterpart, e.g. by simplifying the refinement at the leading edge of the bondline and by reducing number of equations. The FEM codes $\mathscr{F}em2D$, $\mathscr{F}em3D$ and post-processor $\mathscr{X}post$ [4], where used in the evaluations. These softwares have been tested on several benchmark problems in linear and/or non-linear FE analysis. A direct solver based on $\mathbf{L}^T\mathbf{DL}$ factorization was employed to solve the system of algebraic equations obtained from standard finite element mapping.

4. Non-linear viscoelastic response of adhesive

In what follows, the superscript (^{t}) denotes time-dependent quantities, e.g. $\boldsymbol{\varepsilon}^t$ is a time-dependent strain tensor. The constitutive equation for the viscoelastic adhesive was adopted in the form suggested by Schapery [6,7],

$$\boldsymbol{\varepsilon}^t = g_0^{\boldsymbol{\sigma}\theta t} \mathbf{D}_0 \boldsymbol{\sigma}^t + g_1^{\boldsymbol{\sigma}\theta t} \int_0^t \mathbf{J}^{(\psi^t - \psi^{\tilde{\tau}})} \frac{\mathrm{d}}{\mathrm{d}\tilde{\tau}} (g_2^{\boldsymbol{\sigma}\theta\tilde{\tau}} \boldsymbol{\sigma}^{\tilde{\tau}}) \mathrm{d}\tilde{\tau} \qquad (6)$$

where $\mathbf{D}_0$ is the elastic compliance tensor, $\mathbf{J}^t = D_c^{\psi^t} \bar{\boldsymbol{D}}$ is the creep compliance tensor, $D_c^{\psi^t}$ denotes a transient creep compliance function and,

$$\bar{\boldsymbol{D}} = \begin{bmatrix} 1 & -\nu^t & -\nu^t & 0 & 0 & 0 \\ & 1 & -\nu^t & 0 & 0 & 0 \\ & & 1 & 0 & 0 & 0 \\ & & & 2(1+\nu^t) & 0 & 0 \\ & & & & 2(1+\nu^t) & 0 \\ \text{sym.} & & & & & 2(1+\nu^t) \end{bmatrix}. \qquad (7)$$

Table 1
Material properties

	Laminate E-glass/ vinyl ester	Steel AISI 4140 Q&T 650 C	Adhesive Dexter-Hysol EA 9339	Adhesive FM 73
E_{11} [GPa]	22.0	207.0	1.78	2.778
E_{22} [GPa]	22.0	207.0	1.78	2.778
E_{33} [GPa]	8.9	207.0	1.78	2.778
G_{23} [GPa]	3.17	79.0	0.65	1.006
G_{13} [GPa]	3.17	79.0	0.65	1.006
G_{12} [GPa]	5.3	79.0	0.65	1.006
ν_{23}	0.38	0.30	0.37	0.38
ν_{13}	0.38	0.30	0.37	0.38
ν_{12}	0.27	0.30	0.37	0.38
F_{1t} [MPa]	367	–	–	–
F_{2t} [MPa]	367	–	–	–
σ_{ult} [MPa]	–	655	–	50.0

The $g_0^{\boldsymbol{\sigma}\theta t}$, $g_1^{\boldsymbol{\sigma}\theta t}$, $g_2^{\boldsymbol{\sigma}\theta t}$ are non-linear kernel functions of $\boldsymbol{\sigma}^t$ and temperature θ^t, as well as of time t. The function ψ^t is defined by,

$$\psi^t = \int_0^t \frac{\mathrm{d}\tilde{\tau}}{a^{\boldsymbol{\sigma}\theta\tilde{\tau}}}, \tag{8}$$

where $a^{\boldsymbol{\sigma}\theta\tilde{\tau}}$ is a time shift factor. The strain in (6) thus depends on one function of time and four functions of stress and temperature. Specific evaluation of these functions can be derived, for example, for the FM-73 adhesive, using the results by Peretz and Weitsman [8].

As suggested by Henriksen [9] and Reddy and Roy [10, 11], the transient creep function can be expressed by the Dirichlet series,

$$D_c^{\psi^t} = \sum_{r=1}^N D_r[1 - \mathrm{e}^{-\lambda_r \psi^t}], \quad \lambda_r = \frac{1}{\tau_r}, \tag{9}$$

in which τ_r are constant retardation times and N denotes number of Dirichlet coefficients $r \in \langle 1, N\rangle$. The values of D_r, which describe the strain increment during the time period τ_r, can be determined by fitting measured creep curves. The τ_r can be selected subject to certain well-known restrictions. Numerical studies confirmed that the retardation times can be chosen as $\tau_r = 10^{r-2}\tau_2$ for $r = 2, ..., N$, where τ_2 and N have to cover the time range of interest, and $\tau_1 \ll \tau_2$, e.g. $\tau_1 \approx 10^{-5}\tau_2$. The retardation spectrum plotted as $1/D_r$ vs. τ_r $(r = 1, 2, ...N)$ does fully characterize material creep properties [12,13].

Eq. (6) can be expressed in a stress operator form,

$$\boldsymbol{\varepsilon}^t = \mathscr{F}(\boldsymbol{\sigma}^t), \tag{10}$$

where

$$\mathscr{F}(\boldsymbol{\sigma}^t) = \mathscr{J}^t \boldsymbol{\sigma}^t + \mathscr{E}^t, \tag{11}$$

and instantaneous compliance tensor $\mathscr{J}^t$ reads,

$$\mathscr{J}^t = D_I^t \bar{\mathbf{D}}, \quad \mathbf{D}_I^t = g_0^{\boldsymbol{\sigma}\theta t} E^{-1} + g_1^{\boldsymbol{\sigma}\theta t} g_2^{\boldsymbol{\sigma}\theta t} \sum_r D_r(1 - \Gamma_r^t), \tag{12}$$

E is Young's modulus and Γ_r^t is the relaxation coefficient in the creep compliance series,

$$\Gamma_r^t = \frac{1 - \mathrm{e}^{-\lambda_r \Delta \psi^t}}{\lambda_r \Delta \psi^t}, \tag{13}$$

where

$$\Delta \psi^t = \int_{t-\Delta t}^t \frac{\mathrm{d}\tilde{\tau}}{a^{\boldsymbol{\sigma}\theta\tilde{\tau}}}. \tag{14}$$

The hereditary strain component $\mathscr{E}^t$ is defined by

$$\mathscr{E}^t = \bar{\mathbf{D}} g_1^{\boldsymbol{\sigma}\theta t} \sum_r D_r[g_2^{\boldsymbol{\sigma}\theta(t-\Delta t)} \Gamma_r^t \boldsymbol{\sigma}^{t-\Delta t} - \mathrm{e}^{-\lambda_r \Delta \psi^t} q_r^{t-\Delta t}], \tag{15}$$

and the r-th component, $\mathbf{q}_r^{t-\Delta t}$, of the hereditary integral series at the end of the previous load step is

$$\mathbf{q}_r^{t-\Delta t} = \int_0^{t-\Delta t} \mathrm{e}^{-\lambda_r(\psi^{t-\Delta t} - \psi^{\tilde{\tau}})} \frac{\mathrm{d}}{\mathrm{d}\tilde{\tau}}(g_2^{\boldsymbol{\sigma}\theta\tilde{\tau}} \boldsymbol{\sigma}^{\tilde{\tau}})\mathrm{d}\tilde{\tau} \tag{16}$$

The hereditary integral at the end of the current step can be derived from the recurrence formula,

$$\mathbf{q}_r^t = \mathrm{e}^{-\lambda_r \Delta \psi^t} \mathbf{q}_r^{t-\Delta t} + [g_2^{\boldsymbol{\sigma}\theta t} \boldsymbol{\sigma}^t - g_2^{\boldsymbol{\sigma}\theta(t-\Delta t)} \boldsymbol{\sigma}^{t-\Delta t}]\Gamma_r^t, \tag{17}$$

where Γ_r^t is defined by Eq. (13). Once the strain vector (15) is known, the constitutive relation can be written as,

$$\boldsymbol{\sigma}^t = \mathbf{L}^t(\boldsymbol{\varepsilon}^t - \mathscr{E}^t), \quad \mathbf{L}^t = (\mathscr{J}^t)^{-1}, \tag{18}$$

where $\mathbf{L}^t$ is the instantaneous stiffness tensor.

In the finite element implementation of the above theory, the potential energy functional is based on (18),

$$\Pi = \frac{1}{2}\int_\Omega (\boldsymbol{\varepsilon}^t - \mathscr{E}^t)^T \mathbf{L}^t(\boldsymbol{\varepsilon}^t - \mathscr{E}^t)\mathrm{d}\Omega - \int_\Omega \mathbf{u}^T \bar{\mathbf{X}}\mathrm{d}\Omega - \int_\Gamma \mathbf{u}^T \bar{\mathbf{p}}\mathrm{d}\Gamma. \tag{19}$$

After executing the partial derivative of Π with respect to the vector $\mathbf{u}^t$, and using standard isoparametric finite element mapping [14], one obtains a system of algebraic equations,

$$\mathbf{K}^t \mathbf{d}^t = \mathbf{R}^t + \mathbf{R}_{\mathscr{E}}^t \tag{20}$$

where $\mathbf{K}^t$ is the symmetric, positive definite global stiffness matrix after assembly and imposing the essential boundary conditions. The $\mathbf{d}^t$ denotes the global vector of free nodal parameters, and $\mathbf{R}^t$ is the vector of nodal forces due to externally applied mechanical loading and thermal effects. The load vector $\mathbf{R}_{\mathscr{E}}^t$ associated with viscoelastic strain $\mathscr{E}^t$ is given by,

$$\mathbf{R}_{\mathscr{E}}^t = \int_\Omega \mathbf{B}^T \mathbf{L}^t \mathscr{E}^t \mathrm{d}\Omega \tag{21}$$

where $\mathbf{B}^T$ denotes strain displacement transformation operator. Note that in the non-linearly viscoelastic case, the $\mathbf{K}^t$ contains embedded non-linear material kernel functions $g_0^{\boldsymbol{\sigma}\theta t}$, $g_1^{\boldsymbol{\sigma}\theta t}$, $g_2^{\boldsymbol{\sigma}\theta t}$ in the matrix $\mathbf{L}^t$.

A modified Newton–Raphson iterative technique was used to solve (20); the incremental displacement $\Delta \mathbf{d}_r^t$ obtained at the end of the r-th iteration is used to update the local displacement for the n-th time step,

$$\mathbf{d}_r^n = \mathbf{d}_{r-1}^n + \Delta \mathbf{d}_r^n. \tag{22}$$

The iteration continues until convergence is achieved at each time step. The initial condition $\mathbf{d}^0 = \mathbf{0}$ was used in the first time step.

The viscoelastic behavior of the FM-73 adhesive [8] can be completely characterized by the compliance function $D_c^{\psi^t}$ shown in Fig. 4, representing the strain $\boldsymbol{\varepsilon}^t$ of adhesive at time t. The non-linear effects for the constant temperature $\theta^t = 303$ K are expressed by means of stress dependent material kernel functions

$$g_0^{\boldsymbol{\sigma}\theta t} = 1 + 0.2\left(\frac{\tilde{\sigma}^t}{\sigma_{\text{ult}}}\right), \tag{23}$$

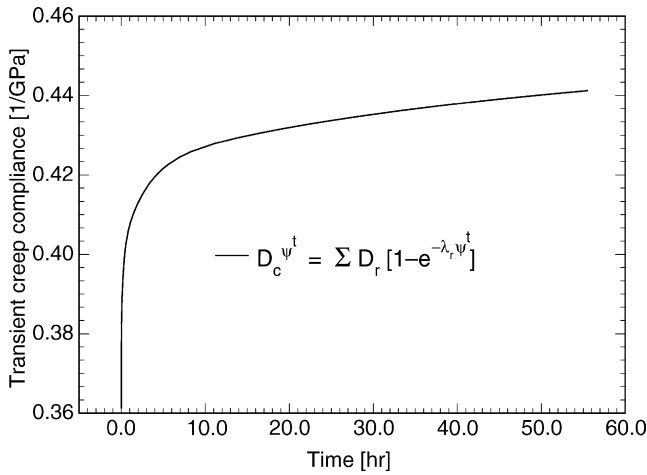$$g_1^{\boldsymbol{\sigma}\theta t} = 1 + 1.435\left(\frac{\tilde{\sigma}^t}{\sigma_{\text{ult}}}\right)^{2.4}, \tag{24}$$

Fig. 4. The transient creep compliance $D_c^{\psi^t}$ represented by (9), calculated for the FM-73 adhesive properties in Table 1.

$$g_2^{\sigma\theta t} = 1 + 0.75\left(\frac{\tilde{\sigma}^t}{\sigma_{ult}}\right)^{2.0}, \tag{25}$$

where the ultimate stress $\sigma_{ult} = 50$ MPa and equivalent Mises stress $\tilde{\sigma}^t = \sqrt{3/2 s_{ij} s_{ij}}$. The shift factor $a^{\sigma\theta\tilde{\tau}}$ is given by

$$a^{\sigma\theta\tilde{\tau}} = e^{-1.5\tilde{\sigma}^t/\sigma_{ult}}. \tag{26}$$

5. Results

Of interest in design are stress distributions and concentrations in the adherends and adhesive at selected sections of the joint. These were obtained for joints of laminate to steel adherends, bonded by either the elastic (D-H 9339) or viscoelastic (FM-73) adhesives. All material properties are listed in Table 1. The D-H 9339 adhesive performed well in our earlier experiments [3], but its inelastic properties have not been determined. Therefore, stress relaxation in the adhesive was examined with the FM-73 system, which has been extensively characterized in the literature [8–10].

The stress distribution in the adherends along the length of the joint is shown in Figs. 5 and 6, which show the longitudinal normal stress, evaluated by 2D analysis, at the lower $x_1 x_2$-surface and the longitudinal mid-section of the two adherends. The 3D analysis produced almost identical results. In Fig. 5, the remotely applied in-plane tension stress $\bar{\sigma}_{11} = 10$ MPa is supported by the solid laminate at the left edge of the graph and by the steel plate at the right edge. Along the joint length, the longitudinal tension stress is distributed between the adherends, but its average in the crossection of the RVE is constant. At points B and C, the adherends are weakened by the groves but not yet joined by the adhesive. Therefore, the total applied force must be supported by the tongue crossection of each adherend. An average stress in the laminate tongue between points $B-E$ is equal to $\sigma_{11}^{laminate} = \bar{\sigma}(17.0/10.5) = 16.19$ MPa, and in
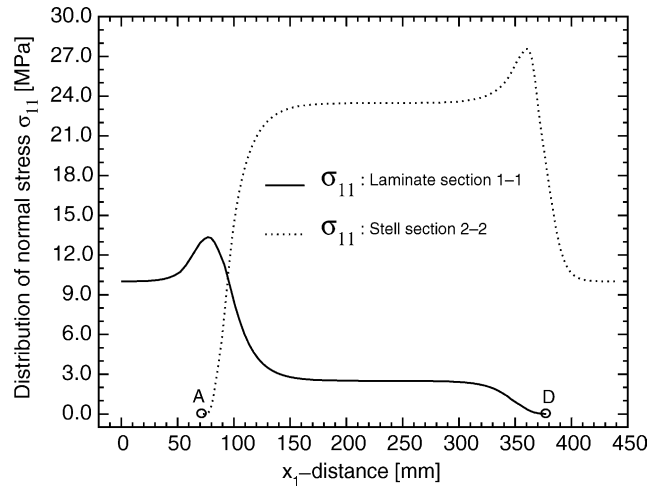

Fig. 5. Longitudinal normal stress σ_{11} caused at the lower surface of the adherends by the tension stress $\bar{\sigma}_{11} = 10$ MPa. As in Fig. 2, Sections 1-1 and 2-2 indicate centerlines of the laminate and steel inserts, respectively. Results calculated with D-H 9339 adhesive properties, Table 1.

the steel tongue between points $F-C$ is equal to $\sigma_{11}^{steel} = \bar{\sigma}(17.0/6.5) = 26.15$ MPa.

Similarly in Fig. 6, under the out-of-plane bending moment M_2, the maximum stress at the bottom surface of remote sections of the plate is equal to $\sigma_{11} = M_2/W = 37.2$ MPa, where $W = bh^2/6$ is the cross section modulus and the values of M_2, b and h are indicated in Figs. 2 and 3. This stress is also shared by the joined adherends, but its average evaluated through the width b must remain constant. The respective averages provide a simple analytical check of the finite element analysis results.

When the joint is loaded only by the in-plane tension stress, the total force applied to the RVEs of Figs. 2 and 3 is found to be 10N/mm^2 × 17 mm × 12.7 mm = 2159 N. This force is transferred between two adherends along the length
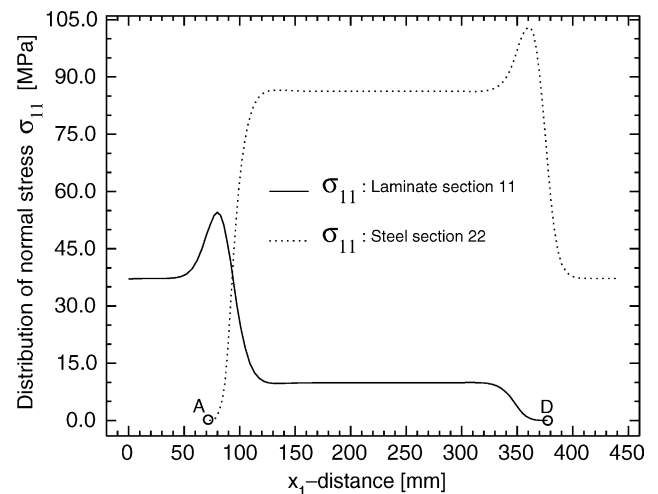

Fig. 6. Longitudinal normal stress σ_{11} caused at the lower surface of the adherends by the bending moment $M_2 = 1 \times 10^{-3}$ MNm/m. As in Fig. 2, Sections 1-1 and 2-2 indicate centerlines of the laminate and steel inserts, respectively. Results calculated with D-H 9339 adhesive properties, Table 1.
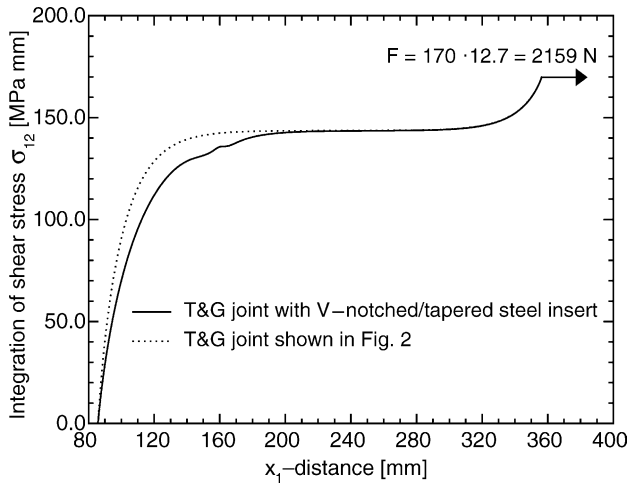
Fig. 7. Transfer of the applied force from the laminate to steel adherends.

of the bondline by the longitudinal shear stress supported by adhesive. Fig. 7 shows this transfer process by showing the distribution of the force transferred from the woven glass-epoxy to the steel tongues forming the joint. The lines shown were obtained by integration of the shear stresses σ_{12}, along the x'-axis in Figs. 2 and 3, from point E to F. The results confirm the well-known rapid rate of transfer from the loaded more compliant composite to the not yet fully loaded but much stiffer steel adherend, cf. Table 1. Of course, this requires that the adhesive supports large shear stresses near its leading edge, which thus becomes the most stressed part of the joint. Tapering the leading edge of the steel adherend, Fig. 3, has a relatively small effect on reduction of the adhesive shear stress under applied tension, but a substantial one (33%) in bending, Tables 3 and 4.

Stress concentrations in the adherends are caused at the leading edges of the adhesive, indicated by points E and F in Figs. 2 and 3. Table 2 shows the stress maxima calculated in the two adherends under tension and bending. Such high stresses were also computed in simulations of the experiments in Ref. [3], where they did not initiate joint failure. Since these stresses are contained in very small material volumes, they are likely to be reduced by an inelastic deformation and/or a localized damage.

At the leading edges E and F of the adhesive in Figs. 2 and 3 the peel stress reaches maximum, and the shear stress maximum is found at a short distance inside the bondline. Tables 3 and 4 show magnitudes of the stress components,

Table 2
Stress maxima at the point E and F of composite and steel adherends, caused by different loading histories at the lower $x_1 x_2$-surface. Values shown are in [MPa], 2D analysis

Stress	Point F-composite adherend		Point E-steel adherend	
	Tension	Bending	Tension	Bending
σ_{11}	44.3	118.3	31.7	105.1

averaged through the thickness of the adhesive layer according to Eq. (5). Note that overall longitudinal tension causes small compressive and tensile peel stresses. The shear stress concentrations are high, comparable in magnitude to the applied stress. Overall bending causes high values of both peel and shear stresses at the leading edge. Comparison of the values in Tables 3 and 4 shows that introduction of the tapered leading edge in Fig. 3 provides stress reductions, which are very substantial in the case of out-of-plane bending of the plate.

To investigate the local stress concentrations, distribution of the adhesive stresses caused by overall bending at the interface in contact with the steel tongue or insert is shown in Fig. 8. This is not a trough-the thickness
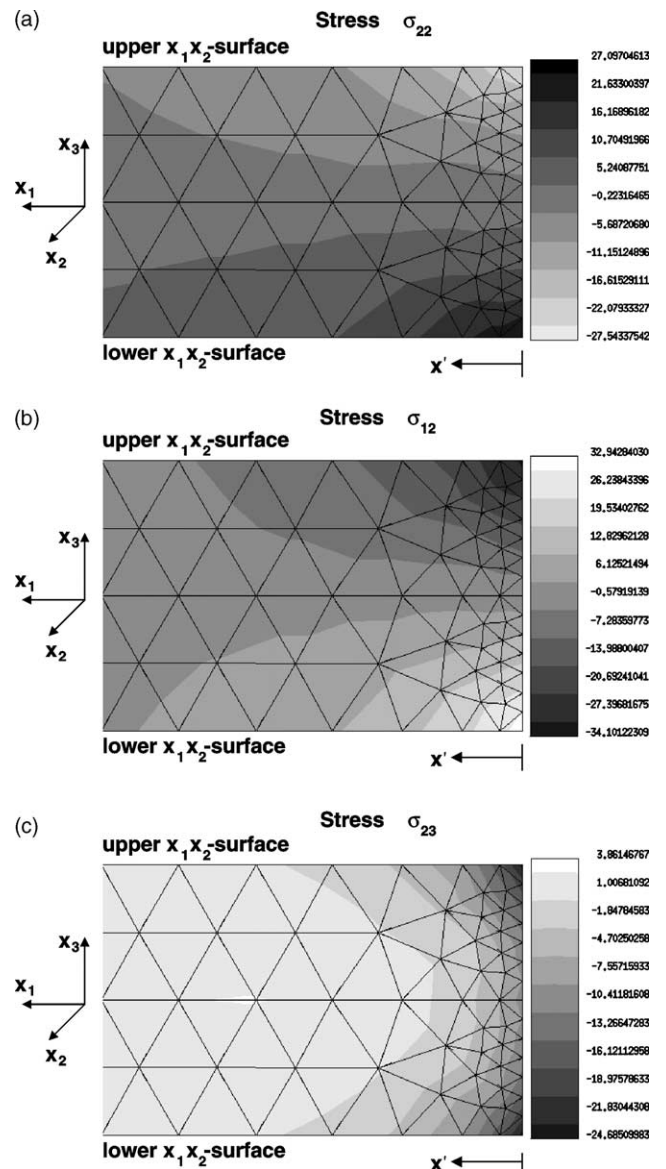

Fig. 8. Distribution of the peel and shear stress components in the adhesive-to-steel-to-insert interface at point E, viewed in the positive x_2 direction in Fig. 2. Loading by the overall bending moment $M_2 = 1 \times 10^{-3}$ MNm/m. Values shown are in [MPa], 3D analysis.

Table 3
Averaged adhesive stress maxima at the point E and F of T&G joint, caused by different loading histories at the lower x_1x_2-surface. Values shown are in [MPa]

Stress	3D Analysis				2D Analysis			
	Point E		Point F		Point E		Point F	
	Tension	Bending	Tension	Bending	Tension	Bending	Tension	Bending
σ_{22}	− 2.94	22.41	0.4	2.8	− 2.37	16.75	0.3	3.2
σ_{12}	13.08	32.14	2.20	6.31	11.50	33.56	2.38	6.19
σ_{23}	0.0	− 24.69	0.0	3.5	0.0	− 21.44	0.0	4.1

average. As expected, maximum values are found at the corner points of the section intersecting point E. Tapering of the stiff steel tongue in the x_1x_3-plane may reduce these values.

Adhesive stress relaxation is shown to be relatively small, and occurring in a short time period as can be seen in Figs. 9 and 10. Response of the viscoelastic adhesive to variable loading histories is illustrated in Figs. 11 and 12. Fig. 11 shows the effective stress strain curve along with loading path cartoon. Here, the non-linear adhesive behavior is observed within first interval following by stress relaxation. The effective Mises stress plotted as a function of time is shown in Fig. 12.

6. Scaling of results to different plate thicknesses

The results of Section 5 suggest that the effect of adhesive viscosity is not very pronounced. Therefore, stress estimates obtained for elastic response of the adhesive can be regarded as conservative for use in design and scaling of the results to different plate thicknesses.

Results computed for a certain thickness of the joined plate can be scaled to a different plate thickness, if the number of bondlines per unit width is retained. This requires keeping the width of the tongues and grooves constant; therefore, the width b of the unit cell used in the original solution is preserved. The change in thickness thus increases the size of the bonded area per unit width, but it has no effect on the in-plane geometry of the joint.

Table 4
Averaged adhesive stress maxima at the point E and F of T&G joint with V-notched/tapered steel insert, caused by different loading histories at the lower x_1x_2-surface. Values shown are in [MPa]

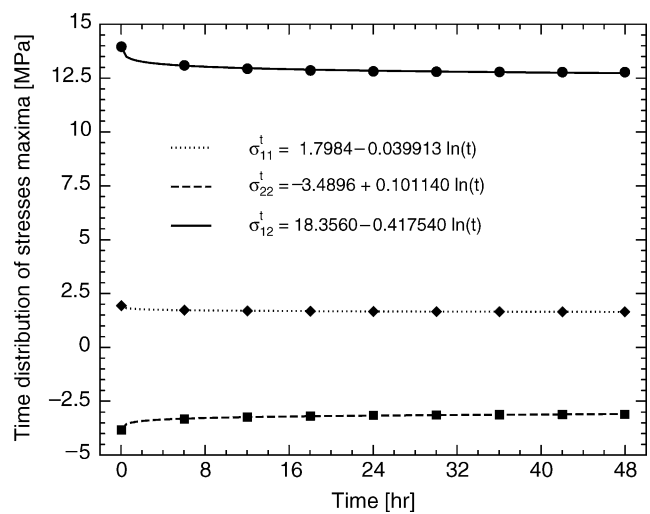| Stress	2D Analysis-T&G joint with V-notch			
	Point E		Point F	
	Tension	Bending	Tension	Bending
σ_{22}	5.43	12.90	0.32	3.2
σ_{12}	10.18	22.88	2.38	6.19
σ_{23}	0.0	− 14.17	0.0	4.6

Fig. 9. Relaxation of maximum stress values at the point E, Fig. 2, of the FM-73 adhesive as a function of time, under sustained loading by the overall tension stress $\bar{\sigma}_{11} = 10$ MPa. Calculated point values are shown together with interpolating lines and their equations.
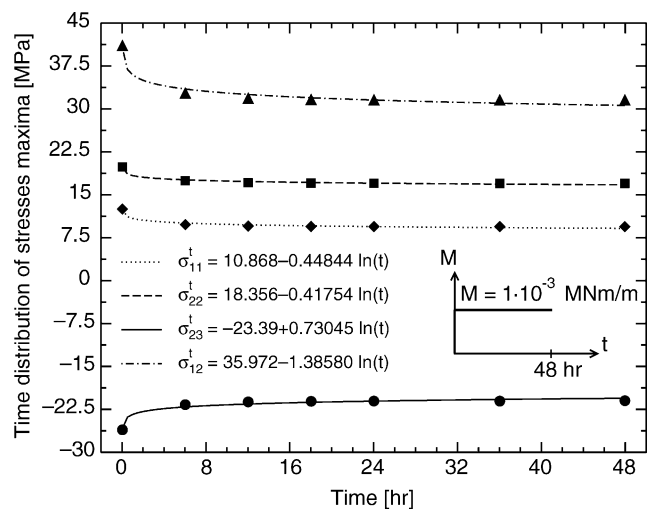
$\sigma_{11}^t = 1.7984 - 0.039913 \ln(t)$
$\sigma_{22}^t = -3.4896 + 0.101140 \ln(t)$
$\sigma_{12}^t = 18.3560 - 0.417540 \ln(t)$

Fig. 10. Relaxation of maximum stress values at the point E of the FM-73 adhesive as a function of time, under sustained loading by the overall bending moment 1×10^{-3} MNm/m. Calculated point values are shown together with interpolating lines and their equations.

$\sigma_{11}^t = 10.868 - 0.44844 \ln(t)$
$\sigma_{22}^t = 18.356 - 0.41754 \ln(t)$
$\sigma_{23}^t = -23.39 + 0.73045 \ln(t)$
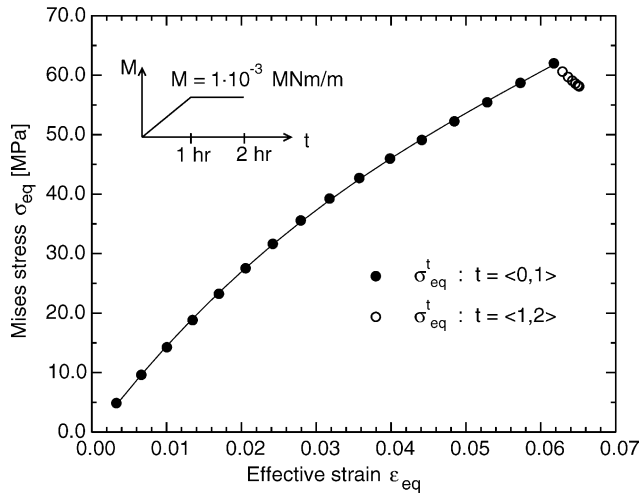$\sigma_{12}^t = 35.972 - 1.38580 \ln(t)$
$M = 1 \cdot 10^{-3}$ MNm/m

Fig. 11. The effective stress–strain behavior at point E of the FM-73 adhesive.

When the plate is loaded by the in-plane normal and by the out-of-plane shear force resultant $\mathbf{N} = [N_{11}, N_{22}, N_{12}]^T$, defined per unit with b in the coordinates of Fig. 1, the overall stress components are obtained as $\boldsymbol{\sigma} = [\sigma_{11}, \sigma_{22}, \sigma_{12}]^T = \mathbf{N}/h$. If the thickness of the plate is changed from an original value h to a new value $h^* = \alpha h$, the overall stress applied by the resultant $\mathbf{N}$ becomes

$$\boldsymbol{\sigma}^* = \frac{\mathbf{N}}{h^*} \equiv \frac{\boldsymbol{\sigma}}{\alpha}. \tag{27}$$

Therefore, if the overall stress is to remain constant after scaling from h to $h^* = \alpha h$, that applied force resultant must be changed from $\mathbf{N}$ to $\mathbf{N}^* = \alpha\mathbf{N}$, also defined per the unit width b.

For loading of the plate by a bending moment M_2 indicated in Fig. 1, the longitudinal normal stress derived from Mindlin's beam theory is $\sigma_{11} = 6\,M_2/(bh^2)$.

Fig. 12. Time distribution of the Mises stress at point E of the FM-73 adhesive.

If the thickness is changed to $h^* = \alpha h$, the stress will become

$$\sigma_{11}^* = \frac{6M_2}{b(h^*)^2} \equiv \frac{\sigma_{11}}{\alpha^2}. \tag{28}$$

To keep the stress σ_{11} constant, the applied moment must be changed from M_2 to $M_2^* = \alpha^2 M_2$.

As long as the T&G joint can be regarded as a stress concentrator in the plate, loading of the plate of a new thickness h^* by a new in-plane force resultant N^* and a bending moment M_2^* will generate the same stresses in the joint as did the original loads N and M_2 in the plate of a thickness h.

7. Conclusions

The results illustrate the stress distributions encountered in adhesive tongue and grove joints of thick laminated composite plates. As in other joint configurations, the stress concentrations at the adhesive leading edge depend on the local geometry of the adherends. However, for given values of stresses in plate sections removed from the joint, the stresses in the joint remain independent of a plate thickness. This is a significant advantage that does not hold in conventional lap joints, and thus favors use of tongue and grove joints of different configurations [2,3] in joining of thick laminates, where the unavoidable stress concentrations at the adhesive leading edge can be amply supported by the high in-plane strength of the laminated plate. Consideration of the viscoelastic response of the adhesive indicates a relatively small relaxation of the local stresses, within a fairly short time period.

References

[1] Hart-Smith LJ. Further developments in the design and analysis of adhesively bonded composite joints. Joining Compos Mater, ASTM-STP 1981;749:3–31.
[2] Bahei-El-Din YA, Dvorak GJ. New designs of adhesive joints for thick composite laminates. Compos Sci Technol 2001;61(1): 19–40.
[3] Dvorak GJ, Zhang J, Canyurt O. Adhesive tongue and groove joints for thick composite laminates. Compos Sci Technol 2001;61: 1123–42.
[4] Matouš K. Anal Optimization Compos Mater Struct, CTU Reports, Prague 2000;4(No. 3/2000).
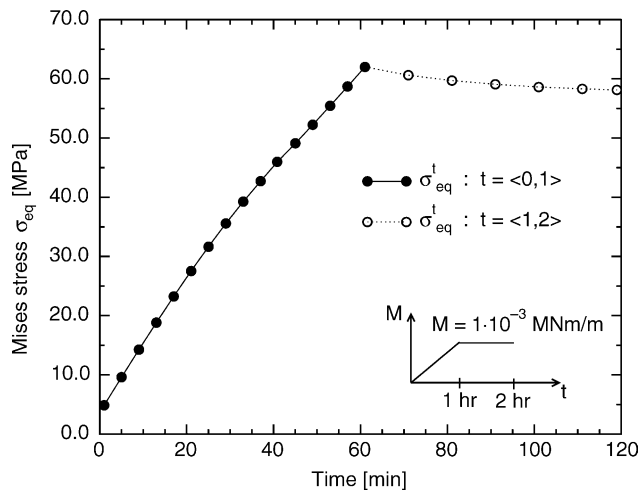[5] Rypl D. Sequential Parallel Generation Unstruct 3D Meshes, CTU Report, Prague 1998;3.

[6] Schapery RA. A method of viscoelastic stress analysis using elasticsolutions. J Franklin Inst 1965;279:268–89.

[7] Schapery RA. On the characterization of non-linear viscoelastic materials. Polym Eng Sci 1969;9(4):295.

[8] Peretz D, Weitsman Y. Nonlinear viscoelastic characterization of FM-73 adhesive. J Rheol 1982;26(3):245–61.

[9] Henriksen M. Nonlinear viscoelastic stress analysis—a finite element approach. Comput Struct 1984;18(1):133–9.

[10] Roy S, Reddy JN. Finite-element models of viscoelasticity and diffusion in adhesively bonded joints. Int J Num Methods Eng 1988; 26:2531–46.

[11] Reddy JN, Roy S. Finite-element analysis of adhesive joints. In: Lee LH, editor. Adhesive bonding. New York: Plenum Press; 1991. p. 359–94.

[12] Bažant ZP, Prasannan S. Solidification theory for concrete creep. II: verification and application. J Eng Mech 1989;115(8):1704–25.

[13] Bažant ZP, Xi Y. Continuous retardation spectrum for solidification theory of concrete creep. J Eng Mech 1995;121(2):281–7.

[14] Hughes TJR. The finite element method, linear static and dynamic finite element analysis. New Jersey: Prentice-Hall, Inc. A Division of Simon and Schuster; 1987.